Earth and Planetary Science Letters 479 (2017) 192–205

Contents lists available at ScienceDirect

Earth and Planetary Science Letters

www.elsevier.com/locate/epsl

Olivine-hosted melt inclusions as an archive of redox heterogeneity in magmatic systems

Margaret E. Hartley [a,*], Oliver Shorttle [b,c], John Maclennan [b], Yves Moussallam [d], Marie Edmonds [b]

[a] School of Earth and Environmental Sciences, University of Manchester, Oxford Road, Manchester, M13 9PL, UK
[b] Department of Earth Sciences, University of Cambridge, Downing Street, Cambridge, CB2 3EQ, UK
[c] Institute of Astronomy, University of Cambridge, Madingley Road, Cambridge, CB3 0HA, UK
[d] Department of Geography, University of Cambridge, Downing Place, Cambridge, CB2 3EN, UK

ARTICLE INFO

Article history:
Received 2 May 2017
Received in revised form 11 September 2017
Accepted 11 September 2017
Available online 3 October 2017
Editor: T.A. Mather

Keywords:
oxygen fugacity
Fe-XANES
melt inclusion
sulfide
melt mixing
Iceland

ABSTRACT

The redox state of volcanic products determines their leverage on the oxidation of Earth's oceans and atmosphere, providing a long-term feedback on oxygen accumulation at the planet's surface. An archive of redox conditions in volcanic plumbing systems from a magma's mantle source, through crustal storage, to eruption, is carried in pockets of melt trapped within crystals. While melt inclusions have long been exploited for their capacity to retain information on a magma's history, their permeability to fast-diffusing elements such as hydrogen is now well documented and their retention of initial oxygen fugacities (fO_2) could be similarly diffusion-limited. To test this, we have measured $Fe^{3+}/\Sigma Fe$ by micro-XANES spectroscopy in a suite of 65 olivine-hosted melt inclusions and 9 matrix glasses from the AD 1783 Laki eruption, Iceland. This eruption experienced pre-eruptive mixing of chemically diverse magmas, syn-eruptive degassing at the vent, and post-eruptive degassing during lava flow up to 60 km over land, providing an ideal test of whether changes in the fO_2 of a magma may be communicated through to its cargo of crystal-hosted melt inclusions.

Melt inclusions from rapidly quenched tephra samples have $Fe^{3+}/\Sigma Fe$ of 0.206 ± 0.008 (ΔQFM of $+0.7 \pm 0.1$), with no correlation between their fO_2 and degree of trace element enrichment or differentiation. These inclusions preserve the redox conditions of the mixed pre-eruptive Laki magma. When corrected for fractional crystallisation to 10 wt.% MgO, these inclusions record a parental magma $[Fe^{3+}/\Sigma Fe]_{(10)}$ of 0.18 (ΔQFM of +0.4), significantly more oxidised than the $Fe^{3+}/\Sigma Fe$ of 0.10 that is often assumed for Icelandic basalt magmas. Melt inclusions from quenched lava selvages are more reduced than those from the tephra, having $Fe^{3+}/\Sigma Fe$ between 0.133 and 0.177 (ΔQFM from -0.4 to $+0.4$). These inclusions have approached equilibrium with their carrier lava, which has been reduced by sulfur degassing. The progressive re-equilibration of fO_2 between inclusions and carrier melts occurs on timescales of hours to days, causing a drop in the sulfur content at sulfide saturation (SCSS) and driving the exsolution of immiscible sulfide globules in the inclusions.

Our data demonstrate the roles of magma mixing, progressive re-equilibration, and degassing in redox evolution within magmatic systems, and the open-system nature of melt inclusions to fO_2 during these processes. Redox heterogeneity present at the time of inclusion trapping may be overprinted by rapid re-equilibration of melt inclusion fO_2 with the external environment, both in the magma chamber and during slow cooling in lava at the surface. This can decouple the melt inclusion archives of fO_2, major and trace element chemistry, and mask associations between fO_2, magmatic differentiation and mantle source heterogeneity unless the assembly of diverse magmas is rapidly followed by eruption. Our tools for understanding the redox conditions of magmas are thus limited; however, careful reconstruction of pre- and post-eruptive magmatic history has enabled us to confirm the relatively oxidised nature of ocean island-type mantle compared to that of mid-ocean ridge mantle.

1. Introduction

Crystal-hosted melt inclusions are a key archive of the geochemical diversity of melts present in magmatic systems, and of

* Corresponding author.
E-mail address: margaret.hartley@manchester.ac.uk (M.E. Hartley).

http://dx.doi.org/10.1016/j.epsl.2017.09.029

the pre-eruptive processes they experience. This chemical diversity is both primary, originating from mantle melting (Dungan and Rhodes, 1978; Sobolev and Shimizui, 1993; Slater et al., 2001) and source heterogeneity (Allègre and Turcotte, 1986; Maclennan, 2008b; Shorttle and Maclennan, 2011), and secondary, originating from differentiation processes in the crust (O'Neill and Jenner, 2012; Brounce et al., 2012; Neave et al., 2014) and degassing of volatile species prior to and during eruption (Métrich and Wallace, 2008). These fundamental magmatic processes have been constrained primarily using the major, trace, and volatile element contents of melt inclusions (Lowenstern, 1995; Sobolev, 1996; Kent, 2008). However, none of these elemental abundances directly record the redox state of the magma as it evolves from mantle source through to eruption.

The clearest tracer of the oxygen fugacity (fO_2) of a magma is its iron oxidation state (Kilinc et al., 1983; Kress and Carmichael, 1991). Whilst traditional bulk wet-chemical methods for determining the relative abundances of Fe^{3+} and Fe^{2+} in a magma, often expressed as $Fe^{3+}/\Sigma Fe$, cannot be applied to melt inclusions, recent advances in synchrotron X-ray absorption near-edge structure (XANES) spectroscopy make it possible to precisely analyse $Fe^{3+}/\Sigma Fe$ on the tens-of-microns scale of melt inclusions (Berry et al., 2003, 2008; Cottrell et al., 2009). In principle, this advance makes it possible to track magmatic fO_2 into the earliest stages of magma formation and evolution (Brounce et al., 2014; Moussallam et al., 2014).

The promise of studying melt inclusions is that, following their entrapment, they are a closed system to subsequent changes in the chemistry of their host magma (Sobolev, 1996; Cherniak, 2010). However, there is now abundant evidence, both experimental and in natural samples, that melt inclusions are open to at least hydrogen exchange with their carrier liquid (Gaetani et al., 2012; Hartley et al., 2015). The key question then is the degree to which the fO_2 of melt inclusions is also modified by post-entrapment processes and changes in the chemical environment.

Melt inclusions are strongly influenced by a range of post-entrapment processes, meaning that inclusions may no longer preserve a record of the fO_2 at which they were formed. Firstly, post-entrapment crystallisation is a near-ubiquitous process in crystal-hosted melt inclusions. For olivine-hosted inclusions, this will sequester Fe^{2+} from the melt into the olivine crystal lattice. Secondly, coupled proton and metal vacancy diffusion through the host olivine allows melt inclusions to approach H_2O and fO_2 equilibrium with their external environment, with complete re-equilibration achieved on timescales of hours to days at magmatic temperatures when the external fO_2 and fH_2O are fixed (Gaetani et al., 2012; Bucholz et al., 2013). The external environment surrounding the melt inclusions, i.e. their carrier melt, is in turn modified by magma mixing (Maclennan, 2008a; Shorttle et al., 2016) and volatile outgassing (Gaillard et al., 2011; Moussallam et al., 2014, 2016; Helz et al., 2017) during storage, ascent and eruption. Coupled with the rapid diffusion of metal vacancies through the host olivine crystal, these processes may mean that initial variability in melt inclusion fO_2 present at the time of entrapment is homogenised.

To investigate the effect of post-entrapment processes on the melt inclusion archive of fO_2, we have made new high-precision measurements of $Fe^{3+}/\Sigma Fe$ by XANES spectroscopy in a suite of 65 naturally quenched olivine-hosted melt inclusions and 9 matrix glasses from the AD 1783 Laki eruption, Iceland. These well-characterised samples provide an opportunity to identify the post-entrapment processes that modify the fO_2 of olivine-hosted melt inclusions. We show that the fO_2 in olivine-hosted inclusions from Laki is principally controlled by diffusive re-equilibration between the inclusion and its external environment: melt inclusions held at high temperatures during magma storage and lava transport approach fO_2 equilibrium with their carrier melt, which itself has an evolving fO_2 in response to magma mixing and degassing of sulfur. We then use the most pristine and least degassed melt inclusion compositions to determine $Fe^{3+}/\Sigma Fe$ and fO_2 in the primary Laki magma. Finally, we assess our dataset for evidence of redox heterogeneity in the diverse melt compositions present at the time of inclusion trapping.

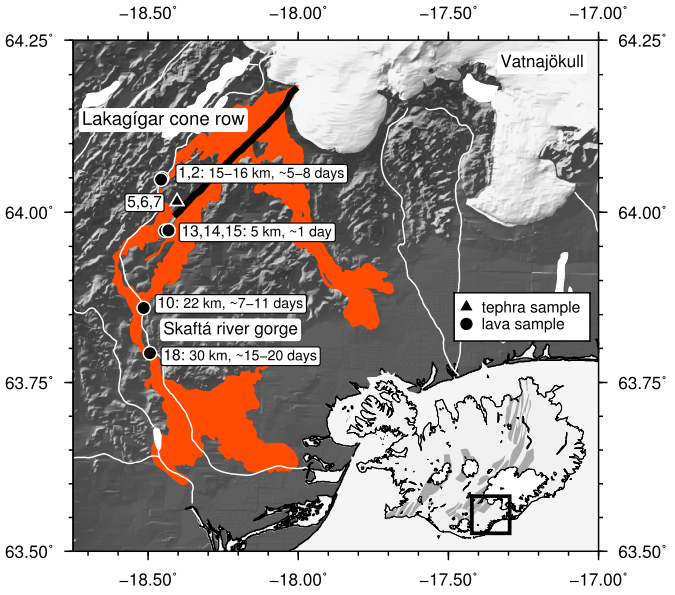

Fig. 1. Map of Iceland's Eastern Volcanic Zone (EVZ) showing the AD 1783 Laki lava flow field. The 27 km-long Laki fissure is shown as a thick black line. Numbered locations show where the samples used in this study were collected. For lava samples, the distance to the source vents and the likely transport time (Hartley et al., 2015) are provided in the sample labels. The inset map shows the location of the EVZ with fissure swarms shaded in dark grey.

2. Methodology

The AD 1783-84 Laki eruption, southeast Iceland, is one of the best-studied small-scale analogues of a flood basalt eruption, and its eruptive history and products have been documented in detail (Métrich et al., 1991; Thordarson and Self, 1993; Thordarson et al., 1996; Guilbaud et al., 2007; Passmore et al., 2012; Neave et al., 2013; Hartley et al., 2016). Our study focuses on a suite of samples that includes both magmatic tephra from the Laki cone row and quenched glassy lava selvages (Fig. 1). The lava selvages were collected at distances of ~5, 15, 22 and 30 km from their source vents, and their melt inclusions are likely to have spent <1 d up to ~15–20 d in insulated lava transport (Hartley et al., 2015). Olivine-hosted melt inclusions and matrix glasses from these samples have previously been analysed for their major, trace and volatile element contents by EPMA, SIMS and Raman spectroscopy (Hartley et al., 2014).

The samples were re-polished to remove pits left by SIMS analysis, then polished on the reverse side to obtain doubly intersected polished wafers in which both sides of the melt inclusions were exposed. Sixty-five previously analysed melt inclusions with obstruction-free areas of at least 10 × 10 μm were selected for XANES analysis.

Fig. 2 shows typical examples of olivine-hosted melt inclusions from tephra and lava samples. Inclusions from tephra samples comprise vitreous, transparent glass with no daughter crystals; some contain a shrinkage bubble, but many are bubble-free (Hartley et al., 2014). Melt inclusions from lava samples are also vitreous, and most contain a vapour bubble. Many lava-hosted in-

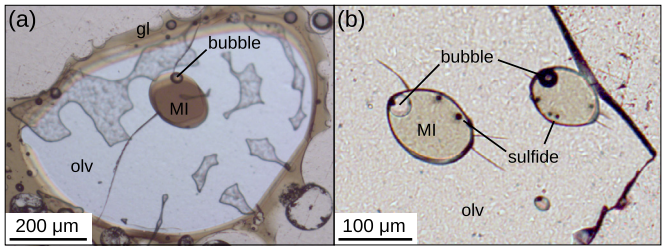

Fig. 2. Transmitted light photomicrographs of olivine-hosted melt inclusions from (a) tephra sample MHL-05, and (b) lava sample MHL-18. The melt inclusions and matrix glass are rapidly quenched and contain no microlites. Melt inclusions in both tephra and lava samples contain vapour bubbles. Melt inclusions from lava samples commonly contain one or more sulfide globules, typically <10 µm in diameter.

clusions contain one or more sulfide globules <10 µm in diameter, but sulfides are very rare in melt inclusions from tephra samples (only one tephra-hosted inclusion was observed to contain a sulfide globule). Twenty-two of the 65 analysed inclusions (21 from lava samples, one from a tephra sample) contained visible sulfides. This is a minimum estimate of the number of sulfide-bearing inclusions, since (a) some of the lava-hosted inclusions without sulfides exposed on the polished surfaces were too dark to see through, and (b) in two lava samples sulfides may have been polished away during sample preparation prior to visual inspection.

Glassy tephra fragments contain acicular plagioclase and clinopyroxene microlites dispersed within visually homogeneous, vitreous glass. The lava selvages contain glassy patches but are more microlite-rich, consistent with having quenched against surface water, such as the Skaftá River, following lava transport. No oxides were present as groundmass crystals in the tephra glasses or lava selvages. Sulfide globules were not observed in the tephra glasses or lava selvages, suggesting that the Laki carrier melt degassed its sulfur before reaching sulfide saturation.

2.1. XANES data acquisition

Synchrotron X-rays were used to probe the pre-edge structure of the Fe K-edge for Laki melt inclusions and matrix glasses. All analyses were performed on beamline I18 at Diamond Light Source (DLS) in a single four-day analytical session in September 2014, during which the storage ring was operating at 3 GeV with an electron current of 200 mA. A 5×3 µm^2 beam was used to measure X-ray intensity over the energy range 7000–7500 eV, using an energy step of 0.1 eV and counting time 10 s over the critical pre-edge interval between 7110 and 7118 eV. Energy step sizes and dwell times are given in Table A.1. The X-ray beam was monochromatised using a (333) reflection of double Si(111) crystals to increase the energy resolution. The sample was held at 45° to the incident X-ray beam and at 45° to the collector, giving an incident-to-fluoresced X-ray angle of 90°. Incident X-ray intensity was measured using a 1.5 cm-long ionisation chamber; fluoresced X-ray intensities were measured using a nine-element germanium detector. The primary X-ray beam was attenuated using either 0.05 mm or 0.1 mm Al plates to keep count rates below the saturation limit of the detector. These analytical conditions translate into a photon flux of $\sim 10^9$ photons/s.

2.2. Beam damage

Previous studies that investigated the effect of beam damage on the Fe K-edge found that prolonged exposure to focused X-ray beams had no effect on Fe speciation under their sets of analytical conditions (Cottrell et al., 2009; Moussallam et al., 2014, 2016). The effect of beam damage under similar analytical conditions at DLS, but with a storage ring current of 300 mA, was tested by Shorttle et al. (2015) using basalt glasses from the Reykjanes Ridge which have similar compositions and H_2O contents to the Laki melt inclusions. They noted a very small photo-oxidation effect over the first 700 s of an analysis, but only when the sample was exposed to an unattenuated X-ray beam. This photo-oxidation effect is barely detectable above the instrument stability and is at least three orders of magnitude less than the variability within our dataset. Given that all our measurements were made using an attenuated beam and whilst the storage ring was operating at a reduced current of 200 mA, we are confident that the iron in our samples was neither oxidised nor reduced during analysis.

2.3. Spectral calibration and fitting of the pre-edge

The XANES spectra were processed and calibrated following the method described by Shorttle et al. (2015). The energy calibration for the spectra was provided by the first derivative peak on an iron foil, 7112.0 eV, measured at the start of the analytical session. Spectra were then normalised to an edge step of 1 by taking the average intensity over the region 7250–7400 eV, in order to avoid incorporating high-amplitude oscillations of the post-edge spectrum in the normalisation (Fig. A.1).

The Smithsonian Institution National Museum of Natural History's basalt reference block NMNH 117393 (Cottrell et al., 2009) was used to calibrate $Fe^{3+}/\Sigma Fe$ in the unknown sample spectra. Calibration was performed using principal component regression (PCR), which uses conventional principal component analysis to identify the spectral features corresponding to the maximum variance in the dataset (Shorttle et al., 2015). The PCR calibration was performed simultaneously on all sample and reference spectra over the energy interval 7105–7119 eV, i.e. the energy of the $1s \rightarrow 3d$ pre-edge transition, such that the calculated principal components form a common basis for the entire dataset. The first principal component (PC1) in this energy range describes >99% of the total variance in the dataset; the second principal component (PC2) describes a peak at ~7114.5 eV, i.e. the second of the two peaks in the pre-edge multiplet. Since both principal components are linearly correlated with $Fe^{3+}/\Sigma Fe$, reference spectra can be used to generate a linear mixing model able to calibrate for $Fe^{3+}/\Sigma Fe$ in the unknown samples.

We used a second principal component regression over the energy interval 7127–7300 eV to identify structure in the edge and post-edge region of the spectra indicative of olivine contamination (Fig. A.2). Ten melt inclusion analyses were deemed to be contaminated by their host olivine on the basis of high PC2 scores in this energy range (Fig. A.2). These measurements were discarded, and six of the inclusions were successfully re-analysed, eliminating the olivine contamination signature. Five matrix glass analyses were rejected on the basis of significant structure in the energy interval 7200–7500 eV indicative of the presence of microlites.

The NMNH reference glasses were analysed three times during the session to monitor analytical drift, which was shown to be negligible. The 2σ reproducibility calculated from these repeat analyses is ~0.3%, and we use an average spectrum for each reference glass in the final PCR calibration. Propagating the error matrix for the PCR calibration parameters through to $Fe^{3+}/\Sigma Fe$ yields an external 2σ precision of 0.8% (absolute).

3. Results

We obtained a total of 65 XANES measurements on Laki melt inclusions and nine measurements on matrix glasses: four from glassy tephra and five from lava selvages. Measured $Fe^{3+}/\Sigma Fe$ in the melt inclusions ranged from 0.135 to 0.234, and there is

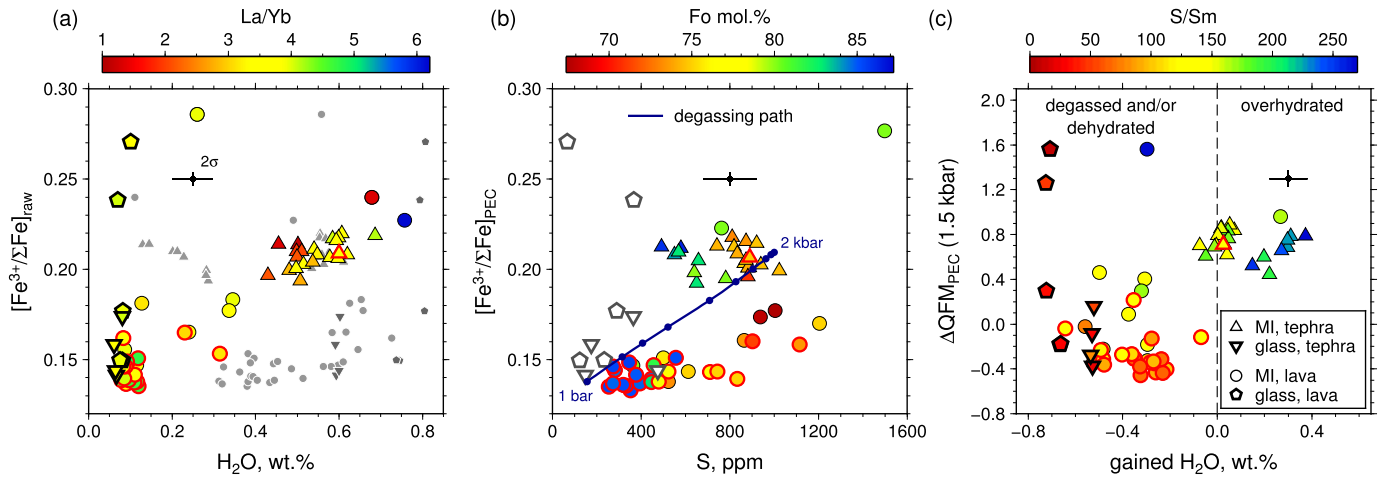

Fig. 3. XANES determinations of $Fe^{3+}/\Sigma Fe$ for Laki melt inclusions and glasses. In all figures, symbols with red outlines indicate melt inclusions containing visible sulfides. (a) Measured $Fe^{3+}/\Sigma Fe$ vs. measured H_2O contents of the analysed samples, coloured by La/Yb. Small grey symbols show the predicted initial H_2O contents of the inclusions and glasses, calculated using Ce as a proxy for H_2O and assuming $H_2O/Ce = 180$. (b) $Fe^{3+}/\Sigma Fe$ of melt inclusions after correction for post-entrapment crystallisation vs. sulfur content, and coloured by host olivine composition. The dark blue line shows the degassing path calculated using the model of Gaillard et al. (2011). Tephra-hosted melt inclusions plot close to the degassing trend. Lava-hosted inclusions lie below the degassing trend and have a limited range in $[Fe^{3+}/\Sigma Fe]_{PEC}$, consistent with a post-eruptive approach towards equilibrium with a degassed carrier melt. (c) Melt inclusions and glasses projected to their $\log(fO_2)$ relative to the QFM buffer, vs. the amount of H_2O gained by post-entrapment H^+ diffusion through the host olivine (see text for details), and coloured by S/Sm. Volatile and trace element data are from Hartley et al. (2014). (For interpretation of the references to colour in this figure, the reader is referred to the web version of this article.)

no progressive variation in $Fe^{3+}/\Sigma Fe$ as a function of distance from the vent. One inclusion was significantly more oxidised with $Fe^{3+}/\Sigma Fe$ of 0.286; this inclusion was situated at the edge of its host olivine and is likely to represent an embayment that remained open to the external melt until shortly before quenching. Seven matrix glasses had $Fe^{3+}/\Sigma Fe$ between 0.141 and 0.177; the other two measurements on lava selvages were significantly more oxidised at 0.238 and 0.271 (Fig. 3a). The three most oxidised lava glasses were measured in a sample collected ~30 km from its source vent; the two more reduced lava glasses were collected ~5 km from the vents (Fig. 1).

The Laki melt inclusions have undergone minor post-entrapment crystallisation (PEC) of olivine onto the melt inclusion walls (Hartley et al., 2014). Tephra-hosted inclusions are affected by an average 1.5% PEC by weight (range 0.2–4.1%); lava-hosted inclusions are affected by a slightly higher average 1.9% PEC (range 0.8–4.8%). Major element compositions were corrected for PEC using Petrolog3 (Danyushevsky and Plechov, 2011), with the olivine-liquid equilibrium model of Gaetani and Watson (2002) and assuming that Fe^{3+} is perfectly incompatible in olivine. The effect of PEC on melt inclusion $Fe^{3+}/\Sigma Fe$ was then corrected by diluting the Fe^{3+} measured by XANES by the calculated extent of PEC, and re-calculating $Fe^{3+}/\Sigma Fe$ according to the PEC-corrected major element composition of the inclusion. The largest PEC correction resulted in a 4.2% (absolute) change in $Fe^{3+}/\Sigma Fe$ (Fig. 3b). We then used Equation (7) of Kress and Carmichael (1991) to project PEC-corrected melt inclusions to their $\log(fO_2)$ relative to the QFM buffer at 1150 °C and 1.5 kbar (Fig. 3c, where the QFM buffer is defined by Frost (1991)), which are taken as representative conditions of pre-eruptive magma storage and final equilibration between crystals and melt (Neave et al., 2013). Matrix glasses were projected to their $\log(fO_2)$ relative to QFM at 1120 °C and atmospheric pressure, representative of magmatic conditions at the point of eruption (Guilbaud et al., 2007). The similar enthalpy and volumes of reaction between the melt iron redox exchange and that of the QFM buffer mean that these small shifts in reference state do not translate into differences in buffer-relative fO_2 (Kress and Carmichael, 1991).

Following PEC correction, $Fe^{3+}/\Sigma Fe$ in tephra-hosted melt inclusions is tightly clustered (Fig. 3b), with a mean value of 0.206 ± 0.008 (1σ). Most inclusions from lava samples are more reduced, with $Fe^{3+}/\Sigma Fe$ between 0.133 and 0.177 (mean 0.147 ± 0.012, 1σ); three lava-hosted inclusions are more oxidised than the tephra-hosted population (Fig. 3b). Within each of the lava- and tephra-hosted melt inclusion populations, there is no difference in $Fe^{3+}/\Sigma Fe$ between melt inclusions that contain visible sulfides and those that do not. There is no relationship between melt inclusion $Fe^{3+}/\Sigma Fe$ and ratios of highly to moderately incompatible trace element ratios such as La/Yb (Fig. 3a) which record trace enrichment in primary melts (Maclennan, 2008a) and their mantle source lithology (Shorttle and Maclennan, 2011). Similarly, there is no statistically significant relationship between melt inclusion $Fe^{3+}/\Sigma Fe$ and host olivine forsterite content (Fig. 3b).

3.1. $Fe^{3+}/\Sigma Fe$, H_2O, and the oxidation state of the pre-eruptive Laki magma

Both raw and PEC-corrected melt inclusion data show a positive correlation between $Fe^{3+}/\Sigma Fe$ and H_2O (Fig. 3a). At first appearance this trend is indicative of progressive oxidation and H_2O enrichment during fractional crystallisation at pressures higher than that required for vapour saturation. However, this cannot be the case, because there is no correlation between the composition of the host olivine and melt inclusion oxidation state (3b). Furthermore, the measured H_2O contents of the Laki melt inclusions are controlled by diffusive re-equilibration with their external carrier melt (Hartley et al., 2015). Experimental studies and numerical modelling have demonstrated that both H_2O and fO_2 in olivine-hosted melt inclusions may completely re-equilibrate with their external environment on timescales of hours to days at magmatic temperatures (Gaetani et al., 2012; Bucholz et al., 2013).

The extent of diffusive H^+ loss or gain experienced by any inclusion can be calculated by taking its Ce concentration as a proxy for the initial H_2O content at the time of inclusion trapping, and assuming a constant H_2O/Ce ratio for undegassed, unmodified melts ($H_2O/Ce = 180 \pm 20$ for basalts from the EVZ; Hartley et al., 2015). Depleted melt inclusions are expected to have the lowest H_2O contents at the time of inclusion trapping, but when mixed with more enriched, hydrous melts in the crust, these inclusions will become hydrated by diffusive gain of H^+ from their new exter-

nal environment. Conversely, enriched inclusions with high initial trapped H_2O contents will lose H^+ if they are incorporated into a drier or degassed melt.

The extent of diffusive H_2O gain (or loss) experienced by the Laki inclusions is shown in Fig. 3c. The measured tephra-hosted inclusions are bimodally distributed: some inclusions are compositionally similar to the Laki carrier melt; the remainder are hosted in $Fo_{>82}$ olivines, have depleted compositions, and have been diffusively hydrated. The reason for the bimodal distribution in the tephra-hosted inclusions is not clear, but may represent a sampling bias that might not persist if more inclusions were measured (Hartley et al., 2014). While it is clear that only those tephra-hosted inclusions with compositions similar to the carrier melt preserve H_2O contents that are unmodified by diffusion, the tephra-hosted inclusions are quenched rapidly enough to preserve a record of the pre-eruptive magmatic H_2O content (0.57 ± 0.05 wt.% H_2O; Hartley et al., 2015). Since the tephra melt inclusions all span a relatively narrow range in $Fe^{3+}/\Sigma Fe$, we conclude that these inclusions also preserve a record of the redox conditions in the Laki magma at its final stage of pre-eruptive equilibration and storage.

The tephra-hosted melt inclusions have a mean ΔQFM of $+0.7 \pm 0.1$ (1σ) (Fig. 3c). The main population of lava-hosted melt inclusions have ΔQFM between -0.1 and -0.5. For all melt inclusions, the PEC-corrected $Fe^{3+}/\Sigma Fe$ and calculated $\log(fO_2)$ are more oxidised than the values of $Fe^{3+}/\Sigma Fe = 0.10$ and ΔQFM-1 that are often taken as representative of Icelandic basalts (Óskarsson et al., 1994; Maclennan et al., 2003; Hartley and Thordarson, 2013; Neave et al., 2013). Even accounting for uncertainties in the Mössbauer calibration of the NMNH standards that may affect the accuracy of XANES measurements (Hirschmann et al., 2015, and Appendix C), an important result of this study is that more evolved Icelandic basalts such as Laki are significantly more oxidised than has previously been recognised.

4. Discussion

4.1. fO_2 modification in Laki melt inclusions

Most of the lava-hosted melt inclusions and matrix glasses have lower H_2O and are significantly more reduced than the tephra-hosted melt inclusions (Fig. 3). This indicates that melt inclusions in crystals that were transported in lava flows have undergone both diffusive dehydration and reduction as they attempt to maintain equilibrium with a progressively reducing and degassing carrier melt.

Modification of H_2O and $Fe^{3+}/\Sigma Fe$ in olivine-hosted melt inclusions proceed according to the following reactions. Proton exchange through the host olivine can occur through the oxidation (or reduction) of Fe on an octahedral lattice site and the creation (or destruction) of two OH^- defects associated with an octahedral site metal vacancy (Kohlstedt and Mackwell, 1998):

$$2H_{melt} + 2Fe^{\bullet}_{Me} + 2O^{\times}_{O} + V''_{Me} = \{(OH)^{\bullet}_{O} - V''_{Me} - (OH)^{\bullet}_{O}\} + 2Fe^{\times}_{Me} \quad (1)$$

Oxygen exchange can occur through the reduction of Fe on an octahedral site and the creation of an octahedral site metal vacancy (Nakamura and Schmalzried, 1983):

$$O_{melt} + \frac{1}{2}[SiO_2]_{melt} + 3Fe^{\times}_{Me} = V''_{Me} + 2Fe^{\bullet}_{Me} + \frac{1}{2}Fe_2SiO_4 \quad (2)$$

In the Kröger–Vink notation for point defects, the subscript indicates the lattice site and the superscript indicates the effective charge ($\times$ = neutral, $\bullet$ = positive charge, $'$ = negative charge). Thus, $Fe^{\times}_{Me}$ and $Fe^{\bullet}_{Me}$ are respectively Fe^{2+} and Fe^{3+} occupying octahedral lattice sites; $O^{\times}_{O}$ and $(OH)^{\bullet}_{O}$ are respectively O^{2-} and OH^- occupying oxygen sites, and V''_{Me} is an octahedral site metal vacancy. Curly brackets denote associated point defects.

Reactions (1) and (2) are both rate-limited by metal vacancy diffusion through the host olivine, and occur on similar timescales (Wanamaker, 1994; Gaillard et al., 2003; Portnyagin et al., 2008; Chen et al., 2011). By combining these reactions, it is possible for melt inclusion H_2O contents to approach equilibrium with their external environment through the incorporation of stoichiometric H_2O into the olivine (Gaetani et al., 2012):

$$H_2O_{melt} + \frac{1}{2}[SiO_2]_{melt} + Fe^{\times}_{Me} + 2O^{\times}_{O} = \{(OH)^{\bullet}_{O} - V''_{Me} - (OH)^{\bullet}_{O}\}^{\times} + \frac{1}{2}Fe_2SiO_4 \quad (3)$$

This reaction is independent of $Fe^{\bullet}_{Me}$, and so it can also be written for forsteritic olivine, Mg_2SiO_4. Re-equilibration of H_2O between a melt inclusion and its external environment therefore involves creation (or destruction) of point defects coupled with growth (or dissolution) of olivine on the inclusion walls. Re-equilibration of fO_2 requires the creation, diffusion and destruction of point defects according to Eq. (2). Note that melt inclusion hydration (or dehydration) is driven by equilibration across a water activity gradient, aH_2O, as opposed to a concentration gradient. Given that H_2O and fO_2 are exchanging via different reactions we do not expect changing aH_2O in the melt inclusion to directly affect its fO_2 (e.g. Botcharnikov et al., 2005).

We investigated the likely timescales of diffusive H_2O and $Fe^{3+}/\Sigma Fe$ re-equilibration between Laki melt inclusions and the carrier lava using a modified version of the model presented by Bucholz et al. (2013). The model calculates an analytical solution for the isotropic diffusion of protons and metal vacancies through a spherical olivine crystal hosting a spherical melt inclusion at its centre (Qin et al., 1992), and uses the experimentally determined diffusion coefficients $D^{H^+}_{[001]} = 10^{-1.4}\exp[-(258/RT)]$ m^2/s for protons (Demouchy and Mackwell, 2006) and $D_{V_{Me}} = 10^{-11.2}$ m^2/s for metal vacancy diffusion at 1100 °C (Wanamaker, 1994). Concentrations of metal vacancies involved in fO_2 re-equilibration are calculated according to Equation (18) of Dohmen and Chakraborty (2007).

Calculations were run at a temperature of 1120 °C, which is an upper estimate of the temperature of post-eruptive insulated transport within the Laki lava (Guilbaud et al., 2007). We calculated the timescale required for melt inclusions with initial $Fe^{3+}/\Sigma Fe$ in equilibrium with the pre-eruptive Laki magma (i.e. the tephra-hosted melt inclusion average $Fe^{3+}/\Sigma Fe$ of 0.206) to reach their measured $Fe^{3+}/\Sigma Fe$. In some cases the calculated timescale represents complete re-equilibration with the carrier lava; in other cases the melt inclusions cooled below the closure temperature for metal vacancy diffusion before equilibrium was reached. The average calculated timescale for melt inclusions to reach their measured $Fe^{3+}/\Sigma Fe$ was 2.34 ± 1.60 d (Fig. 4). Equivalent calculations for diffusive H^+ loss as inclusions approach equilibrium with their degassed carrier lava are reported by Hartley et al. (2015).

For the 30 lava-hosted inclusions for which both $Fe^{3+}/\Sigma Fe$ and H_2O measurements are available, $Fe^{3+}/\Sigma Fe$ modification occurs on average 2.27 ± 1.92 times faster than H_2O (Fig. 4b). This is consistent with recent experimental studies which have suggested that melt inclusion fO_2 and H_2O equilibration occur via independent mechanisms and that H^+ diffusion is not limited by redox exchange (Gaetani et al., 2012; Bucholz et al., 2013).

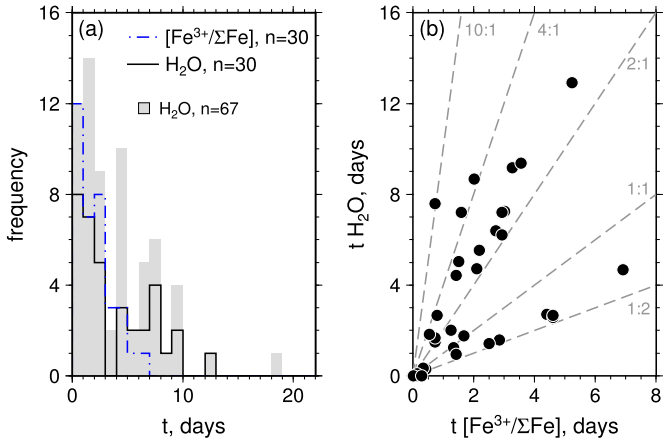

Fig. 4. (a) Timescales of diffusive H_2O (black line) and fO_2 (dashed blue line) exchange between melt inclusions in lava samples and their degassed carrier melt, calculated using the model of Bucholz et al. (2013). Equivalent H_2O re-equilibration timescales from Hartley et al. (2015) are shown by the grey bars. Both H_2O and $Fe^{3+}/\Sigma Fe$ in melt inclusions re-equilibrate with their external environment within hours to days. (b) Re-equilibration of fO_2 occurs more rapidly than re-equilibration of H_2O. Dashed grey lines show lines of constant ratio for H_2O:fO_2 re-equilibration timescales. (For interpretation of the references to colour in this figure, the reader is referred to the web version of this article.)

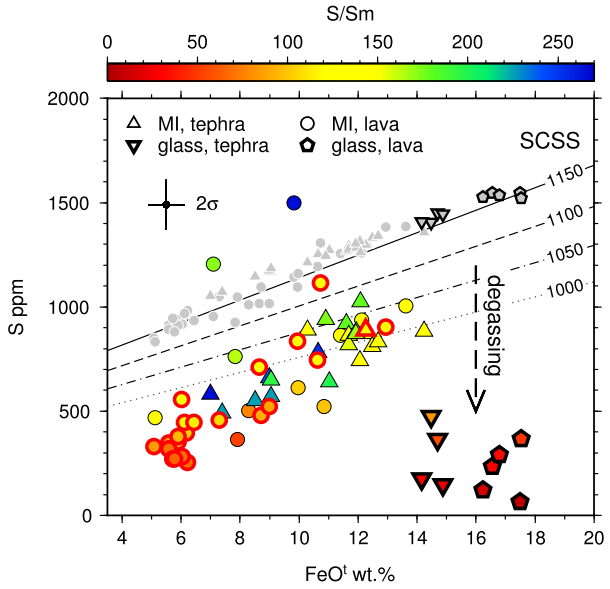

Fig. 5. Measured sulfur contents of Laki samples vs. their total iron content, and coloured by S/Sm. Symbols with red outlines indicate melt inclusions containing visible sulfides. These represent a minimum number of sulfide-bearing inclusions, since the glass in some lava-hosted inclusions was too dark to see through, and in two samples sulfides may have been removed during sample preparation prior to visual inspection. Additionally, some inclusions may have been stored in an oxidised carrier lava prior to quenching, and in this situation the melt inclusion redox state may change sufficiently to re-dissolve any sulfide globules that formed at an earlier stage of its history. Small grey symbols show the sulfur content at sulfide saturation (SCSS; Fortin et al., 2015) calculated at the trapping pressure of each melt inclusion and assuming that inclusions are in H_2O and fO_2 equilibrium with the pre-eruptive carrier melt. The sharp decrease in S at high FeO^t seen in matrix glasses is consistent with sulfur degassing during magma ascent and eruption. Solid and dashed lines show the SCSS at atmospheric pressure and temperatures from 1150 to 1000 °C, calculated using measured H_2O and $Fe^{3+}/\Sigma Fe$ values for each inclusion. (For interpretation of the references to colour in this figure, the reader is referred to the web version of this article.)

4.2. The effect of sulfur degassing

The potential of sulfur outgassing to affect melt oxidation state has been demonstrated both theoretically (Burgisser and Scaillet, 2007; Gaillard et al., 2011) and in nature, where at both Erebus and Kilauea volcanoes, melt reduction is driven by sulfur degassing (Moussallam et al., 2014, 2016; Helz et al., 2017). To explore the possible effects of sulfur degassing on the Laki melt inclusions, we first examined the relationship between $Fe^{3+}/\Sigma Fe$ and measured S contents in the silicate glass.

The main population of melt inclusions from lava samples shows a modest negative correlation between $Fe^{3+}/\Sigma Fe$ and S ($r^2 = 0.61$), while for inclusions from tephra samples we find no correlation (Fig. 3b). Measured sulfur and total iron contents in the melt inclusions are consistent with simple melt fractionation (Fig. 5), suggesting that the inclusions did not trap a progressively degassing melt. Sulfur is not expected to diffuse through the host olivine after inclusion entrapment (although the diffusivity of S in olivine has yet to be examined experimentally). This decouples the records of sulfur and fO_2 in melt inclusions, since fO_2 will continually approach equilibrium with the carrier melt while sulfur remains immobile.

The predicted sulfur content at sulfide saturation (SCSS) for the melt inclusions and glasses, calculated following the method of Liu et al. (2007) with the modifications described by Fortin et al. (2015), suggests that all but two of the Laki melt inclusions were sulfur-undersaturated at the time of inclusion trapping (Fig. 5). In contrast, matrix glasses show low S contents consistent with sulfur outgassing (Fig. 5) and, with the exception of two very oxidised measurements, appear to record a trend of melt reduction in response to sulfur loss (Fig. 3b).

To further explore the effects of volatile outgassing on the Laki melt oxidation state, we used the model of Gaillard et al. (2011) to calculate an equilibrium closed-system degassing path for magma ascent from 2 kbar to atmospheric pressure. At each pressure step the model solves for gas-melt equilibrium in the C–H–S–O system, using thermodynamic data for H_2O and CO_2 from Iacono-Marziano et al. (2012); sulfur from O'Neill and Mavrogenes (2002) and hydrogen from Gaillard et al. (2003). The model starting conditions (pressure = 2030 bar; temperature = 1423.15 K; FeO = 12.6 wt.%; sulfur capacity $\ln C_S = -1.87$, calculated following O'Neill and Mavrogenes (2002); S = 1000 ppm; $fH_2O = 35$ bar; $fH_2 = 0.22$ bar) were selected to be representative of the least degassed melt inclusions from the tephra samples. Results are summarised in Figs. 3b and 6.

The modelled pressure vs. $Fe^{3+}/\Sigma Fe$, S, S/C and H/C trends are very close to that defined by the tephra-hosted melt inclusions and tephra glasses (Fig. 6), and reproduce the observed reduction of the matrix glasses with outgassing. A sub-population of depleted tephra-hosted inclusions have lower S contents than predicted by the degassing trend (Figs. 3b and 6b); however, these inclusions are trapped in $Fo_{>80}$ olivines and their low sulfur contents reflect a primitive, undegassed magma rather than progressive degassing during magma evolution and ascent. The lava-hosted melt inclusions are uniformly offset from the modelled degassing path (Fig. 3b), but this is not surprising given that $Fe^{3+}/\Sigma Fe$ in these inclusions has approached equilibrium with the degassed melt at 1 bar.

Why are two of the quenched glassy lava selvages so oxidised in comparison to the melt inclusions and the modelled degassing trend? The three most oxidised glasses were measured immediately adjacent to large olivine crystals in sample MHL-18 collected ~30 km downstream of the Laki fissure, while the two most reduced lava glasses were measured in samples collected within 5 km of their eruptive vent. The most oxidised lava glasses also have the highest FeO^t contents, indicating a greater extent of microlite crystallisation during insulated transport. We suggest that the oxidised lava glasses represent a combination of olivine and clinopyroxene microlite growth, and interaction of the melt with atmospheric oxygen prior to quenching (Helz et al., 2017).

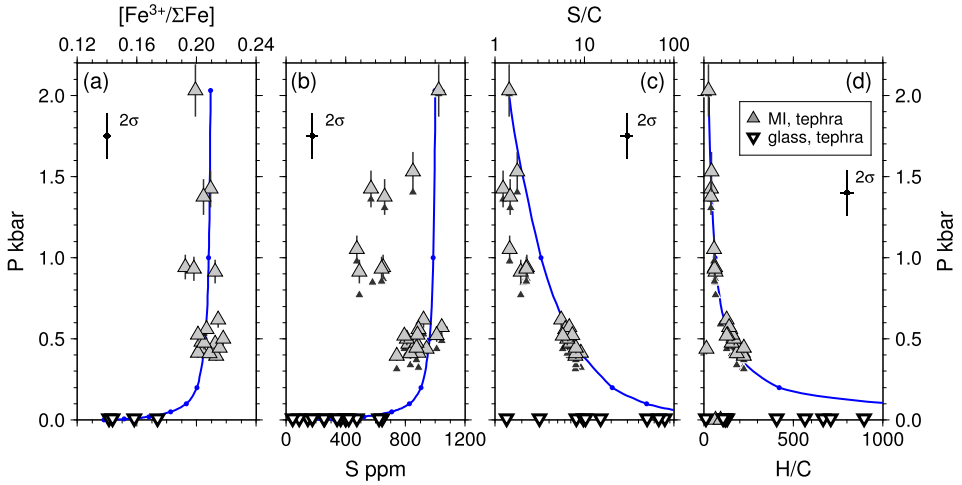

Fig. 6. Degassing pathways of Laki melts, calculated using the model of Gaillard et al. (2011). Calculated decompression and degassing pathways are shown by the blue lines. Melt inclusion saturation pressures were calculated using the volatile saturation model of Iacono-Marziano et al. (2012) and volatile concentrations from Hartley et al. (2014); saturation pressures for the same inclusions calculated using VolatileCalc (Newman and Lowenstern, 2002) are shown by the small black symbols. While a subset of melt inclusions have lower than predicted S contents, the measured melt inclusion and glass compositions are consistent with a model of shallow sulfur degassing controlling the redox evolution of the magma. (For interpretation of the references to colour in this figure, the reader is referred to the web version of this article.)

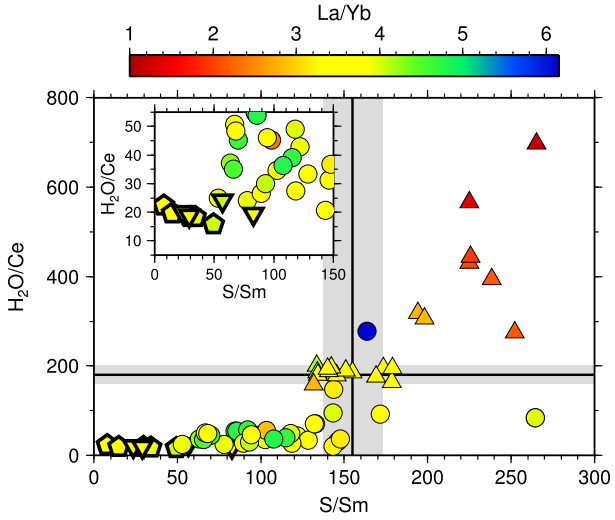

Fig. 7. H_2O/Ce vs. S/Sm for Laki melt inclusions and glasses, coloured by La/Yb. Grey shaded bars indicate the expected values for these ratios in the pre-eruptive Laki magma. Inclusions in the lower left-hand corner have experienced both diffusive dehydration and sulfur loss from the silicate melt phase. Inclusions in the upper right-hand corner have experienced diffusive over-hydration in a more hydrous carrier melt. The range in S/Sm in the upper right-hand corner correlates negatively with La/Yb, and reflects S/Sm heterogeneity in the melts sampled by these inclusions. (For interpretation of the references to colour in this figure, the reader is referred to the web version of this article.)

4.3. fO_2 modification drives sulfide saturation in melt inclusions

Although the Laki melt inclusions are predicted to have been sulfur-undersaturated at the time of inclusion trapping, many of the lava-hosted inclusions have very low S/Sm and S/Dy ratios (Fig. 7). In melt inclusion suites that trap sulfur-undersaturated melts, S is expected to correlate positively with similarly incompatible trace elements such as Sm or Dy (e.g. Saal et al., 2002). This is the case for Laki tephra-hosted inclusions, as shown in Fig. A.3. The tephra-hosted inclusions also sample variable melt compositions at the time of inclusion trapping: a negative correlation between S/Sm and La/Yb ($r^2 = 0.75$) reflects mixing of enriched (high La/Yb, low S/Sm) and depleted (low La/Yb, high S/Sm) primary melts.

Tephra-hosted inclusions with near-identical compositions to the pre-eruptive carrier melt provide a minimum unmodified S/Sm value for the mixed Laki magma of 154 ± 17 (1σ; Fig. 7), but many lava-hosted inclusions have S/Sm significantly lower than this value (Fig. 7). This could be caused by post-entrapment modification of the initial melt S content, but Hartley et al. (2014) found no evidence for sulfur species in Raman spectra of fluid bubbles in these inclusions so post-entrapment S degassing into a fluid phase is unlikely. Similarly, S diffusion through olivine is expected to be negligible. This raises the possibility that S sequestration into a sulfide phase has lowered S/Sm in some Laki melt inclusions.

Experimental studies have demonstrated that silicate melts are able to carry more dissolved S when sulfate, S^{6+}, is the dominant sulfur species, and that the transition from sulfide- to sulfate-dominated systems occurs over a relatively narrow fO_2 interval from approximately $\Delta FMQ = 0$ to $\Delta FMQ + 2$, although this interval depends on the Fe^{2+} content of the melt (Wilke et al., 2011). A recent study of trachyandesitic magmas also implies that sulfate should become increasingly stabilised as pressure decreases (Matjuschkin et al., 2016), although the effect is poorly constrained for basaltic magmas and for pressures <5 kbar. This process also occurs in competition with sulfur outgassing during magma ascent which reduces the melt and stabilises sulfide (Jugo et al., 2010), and it remains unclear whether sulfide or sulfate should be preferentially stabilised for a given magma ascent rate. In the following discussion we have assumed that any pressure-driven stabilisation of sulfate is negligible.

The Laki melt inclusions have redox states within the range $\Delta FMQ = 0$ to $\Delta FMQ + 2$, but inclusions in lava samples are reduced as they attempt to maintain equilibrium with their degassed carrier melt, causing the SCSS to decrease (Jugo, 2009). This may drive the reduced inclusions to sulfide saturation, promoting the formation of immiscible sulfide globules according to the following reaction (Mavrogenes and O'Neill, 1999):

$$FeO^{melt} + \frac{1}{2}S_2^{melt} = FeS^{sulfide} + \frac{1}{2}O_2^{melt} \quad (4)$$

Note that if sulfate is stabilised according to the sulfate-producing reaction

$$\frac{1}{2}S_2 + 2O_2 = [SO_4]^{2-} \quad (5)$$

then reaction 4 can be expressed in terms of a sulfate melt component:

$$FeO^{melt} + [SO_4]^{2-,melt} = FeS^{sulfide} + \frac{5}{2}O_2^{melt} \quad (6)$$

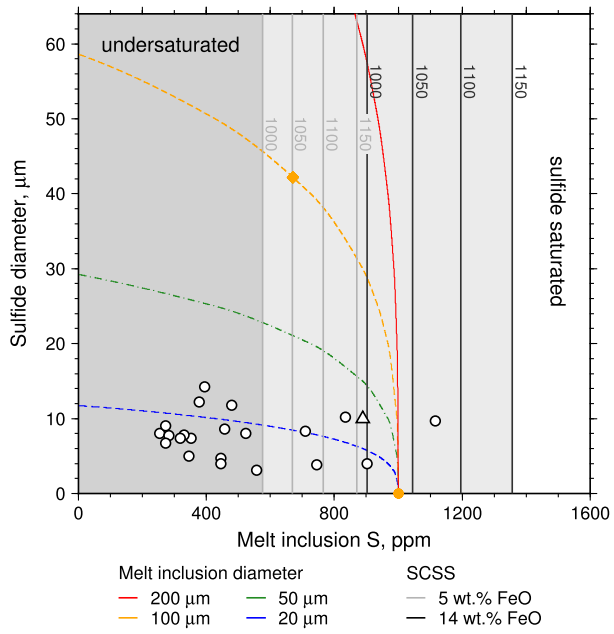

Fig. 8. Modelled sulfide saturation and formation of immiscible sulfide melt globules in a melt inclusion with an initial trapped sulfur content of 1000 ppm. Coloured lines show the theoretical maximum radius of an immiscible sulfide globule and the sulfur content remaining in the silicate melt for inclusions of different radii, assuming that the silicate melt is always sulfide over-saturated and that any exsolved sulfide coalesces into a single globule. Black and grey lines show the sulfur content at sulfide saturation (SCSS) for Laki melt inclusion compositions with 14 and 5 wt.% FeO^t respectively, at temperatures from 1150 to 1000 °C. Melt inclusion compositions with <570 ppm initial trapped sulfur are predicted to remain sulfide undersaturated at magmatic conditions (dark grey shaded area). Melt inclusions with initial trapped S contents >1360 ppm S are sulfide-saturated above 1150 °C, and are predicted to exsolve immiscible sulfide globules. Melt inclusions with intermediate sulfur contents (light grey shaded area) may become sulfide-saturated in response to reduction and cooling. For example, a 100 µm diameter melt inclusion with 5 wt.% FeO and 1000 ppm S (orange circle) is sulfide-undersaturated at 1150 °C, but if cooled to 1050 °C will become sulfide over-saturated and exsolve a 42 µm diameter sulfide globule in order to return the silicate liquid to its SCSS (orange diamond). White symbols show the glass S contents of Laki melt inclusions that contain visible sulfides, and the equivalent sulfide diameter if all exsolved sulfide formed a single globule (note that these are minimum estimates of the sulfide content of the inclusions). (For interpretation of the references to colour in this figure, the reader is referred to the web version of this article.)

Fig. 5 shows clearly that some lava-hosted inclusions may have reached sulfide saturation in response to reduction and post-emplacement cooling. However, tephra-hosted inclusions quenched rapidly on eruption are unlikely to reach sulfide saturation. This is consistent with our observations that immiscible sulfides are common in lava-hosted melt inclusions, but tephra-hosted inclusions are mostly sulfide-free. Lava-hosted inclusions with visible sulfides are marked with red outlines in Fig. 5, and their S contents fall consistently towards the lower end of the measured range in S for any given total iron content.

We used simple mass balance calculations to estimate the maximum volume of immiscible sulfide melt that could be produced by driving melt inclusions with differing radii and initial trapped S contents to sulfide saturation. The sulfide is assumed to form a single spherical globule, although in reality we often observe multiple small sulfides within a single inclusion. The sulfides are assumed to have the same composition as those measured in Reykjanes Ridge glasses (Czamanske and Moore, 1977) and a density of 4200 kg/m^3 (Mungall and Su, 2005); the silicate melt density was taken to be 2750 kg/m^3 (Passmore et al., 2012). An example set of calculations for an inclusion with 1000 ppm S are shown in Fig. 8, along with calculated sulfur contents at sulfide saturation for the most primitive (~5 wt.% FeO^t) and most evolved (~14 wt.% FeO^t) melt inclusion compositions at magmatic temperatures. The SCSS calculations are performed on the basis of total iron under the fO_2 conditions of the pre-eruptive melt, i.e. without simultaneously reducing the magma to simulate redox changes during ascent, eruption and post-eruptive transport, and therefore represent the maximum sulfide solubility at a given temperature. From Fig. 8, any inclusion with an initial trapped S content >1360 ppm is expected to have reached sulfide saturation and exsolved an immiscible sulfide phase. Other inclusions may reach sulfide saturation depending on their total iron content, initial trapped S content, the oxidation state of the external environment, and the temperature.

The melt inclusions with observed sulfides are shown on Fig. 8. The equivalent sulfide diameters shown represent minimum sulfide contents for these inclusions, since we do not know how many sulfide globules were removed during the sample preparation process. While the measured glass S contents are somewhat lower than expected given the calculated SCSS, it is clear that post-entrapment sulfide nucleation in response to reduction and cooling can be achieved within the Laki inclusions. This may explain the low S/Sm values in the lava-hosted melt inclusions.

Post-entrapment crystallisation could also drive sulfide saturation in melt inclusions since PEC raises the S content of the residual melt. A decrease in fO_2 of ~1.3 log units (due to modification by diffusive exchange with a degassed, reduced carrier lava) may have caused the melt inclusion sulfur content to be raised ~100–150 ppm over the SCSS. In comparison, 5% PEC could increase the residual S content of the most sulfur-rich Laki melt inclusions by ~70 ppm and, depending on the total iron content of the trapped melt, lower the SCSS by up to 350 ppm. To explore the effects of PEC on sulfide saturation, we compared the S contents and SCSS for both measured and PEC-corrected melt inclusion compositions. While PEC lowers the predicted SCSS in all Laki melt inclusions, only the three most S-rich lava-hosted inclusions (each with PEC>3%) could have been driven to sulfide saturation by PEC alone. Approach to equilibrium with a reduced external melt is therefore the dominant driving force for sulfide saturation in the Laki inclusions.

4.4. Can olivine-hosted melt inclusions preserve redox heterogeneity in primary melts?

Previous studies of MORB suites analysed by XANES have demonstrated that $Fe^{3+}/\Sigma Fe$ in basaltic magma is sensitive to low-pressure fractionation (Cottrell and Kelley, 2011; Shorttle et al., 2015). To extract information concerning the $Fe^{3+}/\Sigma Fe$ of primary melts supplied to the Laki magmatic system, it is first necessary to remove variation in $Fe^{3+}/\Sigma Fe$ generated by fractional crystallisation.

We used Petrolog3 (Danyushevsky and Plechov, 2011) to correct the Laki glass and PEC-corrected melt inclusions to 10 wt.% MgO. The most primitive melt inclusions analysed from Iceland's Eastern Volcanic Zone to date contain ~10.5 wt.% MgO (Neave et al., 2017), although true primary melts are likely to be more primitive still. Reverse fractional crystallisation paths were calculated assuming a pressure of 2 kbar, using the mineral-melt equilibria of Langmuir et al. (1992). We tested two fractionation correction methods. The first was a single-stage model with no imposed constraints on the crystallising assemblage. The second was a two-stage model whereby at MgO<8 wt.% fractionation occurs in the olivine+plagioclase+clinopyroxene (i.e. gabbro) field, and subsequent correction to 10 wt.% MgO is calculated assuming that olivine is the only crystallising phase (Fig. 9). Both methods gave very similar results. We chose to focus on the two-stage model because this facilitates direct comparison of the Laki melt inclusions with glasses from the Reykjanes Ridge corrected for fractionation using a two-stage model (Shorttle et al., 2015).

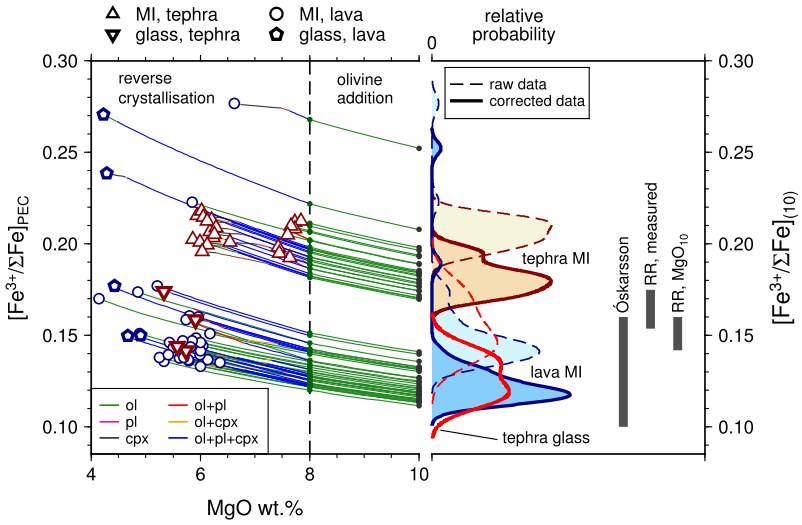

Fig. 9. Reverse fractional crystallisation paths for Laki melt inclusions and tephra glasses. Starting compositions corrected for post-entrapment crystallisation are shown by open symbols, and reverse fractionation paths are shown by the lines extending to higher MgO. At MgO<8 wt.% fractionation occurs in the olivine+plagioclase+clinopyroxene (i.e. gabbro) field, and the crystallising assemblage is indicated by colour. Subsequent reverse fractionation to 10 wt.% MgO is calculated by olivine addition. The right-hand panel shows kernel density estimates (KDEs) of the data: filled blue and beige KDEs show melt inclusions from lava and tephra samples respectively, and unfilled red KDEs shows tephra glass. The dashed lines show KDEs for the starting compositions, and solid lines show the melt compositions corrected to 10 wt.% MgO. For both initial and final datasets, melt inclusions from lava samples have similar compositions to the tephra glass, and both are more reduced than melt inclusions from tephra samples. Grey bars correspond to $Fe^{3+}/\Sigma Fe$ values obtained by Óskarsson et al. (1994) for Icelandic basalts, and Shorttle et al. (2015) for Reykjanes Ridge glasses (measured values, and fractionation-corrected to 10 wt.% MgO). (For interpretation of the references to colour in this figure, the reader is referred to the web version of this article.)

Fractionation-corrected melt inclusions from tephra samples have a mean $[Fe^{3+}/\Sigma Fe]_{(10)}$ of 0.180, compared with a PEC-corrected $Fe^{3+}/\Sigma Fe$ of 0.206 (Fig. 9). In both cases, the variability is ±0.02. Fractionation-corrected tephra glasses and lava-hosted inclusions both have mean $[Fe^{3+}/\Sigma Fe]_{(10)}$ of 0.117 (Fig. 9). However, for tephra glasses the starting $Fe^{3+}/\Sigma Fe$ has been modified by SO_2 degassing, and $Fe^{3+}/\Sigma Fe$ in the lava-hosted inclusions has been modified by diffusive exchange with the degassed carrier melt; therefore only $[Fe^{3+}/\Sigma Fe]_{(10)}$ for tephra-hosted melt inclusions can be used to constrain the primary melt fO_2. As is observed with $[Fe^{3+}/\Sigma Fe]_{PEC}$ (Section 4.1), the fractionation-corrected $[Fe^{3+}/\Sigma Fe]_{(10)}$ of 0.180 for the tephra-hosted melt inclusions is significantly more oxidised than the $Fe^{3+}/\Sigma Fe$ of 0.10 commonly assumed for Icelandic primary melts, and suggests that Laki primary melts must sample a significant contribution from an enriched mantle source component derived from recycled, oxidised oceanic crust (Shorttle et al., 2015). From Fig. 9 it is clear that the best estimation of $Fe^{3+}/\Sigma Fe$ in the primary melts supplying any magmatic system will be achieved by fractionation correction of melt inclusions that are compositionally near-identical to the erupted carrier liquid, and have been rapidly quenched. However, even these inclusions will have experienced pre-eruptive modification as they moved towards equilibrium with their host magma, therefore recording the fO_2 conditions of the mixed pre-eruptive melt rather than the fO_2 at the point of inclusion trapping.

What evidence is there that the tephra-hosted melt inclusions preserve a re-equilibrated fO_2 signal from a mixed pre-eruptive melt? Redox heterogeneity in melt inclusions would be expected from any or all of the following processes: (a) Fractionation of dominantly Fe^{2+}-bearing minerals (e.g. olivine) from the primary melt; (b) Sampling different depths within the mantle melting column (Gaetani, 2016); (c) Sampling lithological heterogenities in the mantle source (Shorttle et al., 2015). In Icelandic magmas many geochemical parameters correlate and so we expect some degree of co-variation between these processes, although this is a subject of ongoing research. Previous work by Shorttle et al. (2015) suggests a positive correlation between mantle source enrichment and $Fe^{3+}/\Sigma Fe$ for Reykjanes Ridge basalts, and more enriched Icelandic basalts are also known to be slightly wetter (Nichols et al., 2002). These changes in primary melt chemistry then map onto differing fractionation trajectories for enriched, depleted and mixed magmas (e.g. Winpenny and Maclennan, 2011).

Melt inclusions from Laki tephra are hosted in olivines that span over 10 mol.% forsterite, thus we might expect their melt inclusions to record changes in $Fe^{3+}/\Sigma Fe$ caused by melt differentiation. However, we see no systematic signal of increasing fO_2 with decreasing host forsterite content (Fig. 10a). Similarly, although trace element ratios such as La/Yb and Nb/Zr record mixing of compositionally diverse melts, they do not appear to record the fO_2 variability that might be expected from mixing reduced depleted, and oxidised enriched primary melts, nor from fractional melting of an isochemical source (Fig. 10b). That the tephra-hosted inclusions do not appear to record the fO_2 heterogeneity predicted by simple melting and differentiation models strongly suggests that the fO_2 at the point of inclusion trapping has been overprinted by re-equilibration within a mixed pre-eruptive melt.

Our results demonstrate that it is challenging to use olivine-hosted melt inclusions to see through the processes of concurrent mixing and crystallisation to recover evidence of redox heterogeneity in the enriched and depleted primary melts supplied to magmatic systems. In the best-case scenario, where melt mixing occurs near-concurrently with ascent and eruption and the erupted products are rapidly quenched, it may be possible to avoid complete overprinting of melt inclusion fO_2 and hence to recover a minimum estimate of redox heterogeneity in the unmixed primary melts. Despite these difficulties, olivine-hosted melt inclusions do provide a reliable archive of the minimum pre-eruptive magmatic fO_2, provided that $Fe^{3+}/\Sigma Fe$ is measured in rapidly quenched tephra or pillow glass samples. Inclusions from olivines that have experienced insulated transport in a lava flow can be used to track the post-eruptive redox evolution of the magma as it degases sulfur to the atmosphere.

5. Conclusions

We have investigated the pre- and post-eruptive redox evolution of a major basaltic eruption to understand what information on mantle redox is retained through magmatic processing.

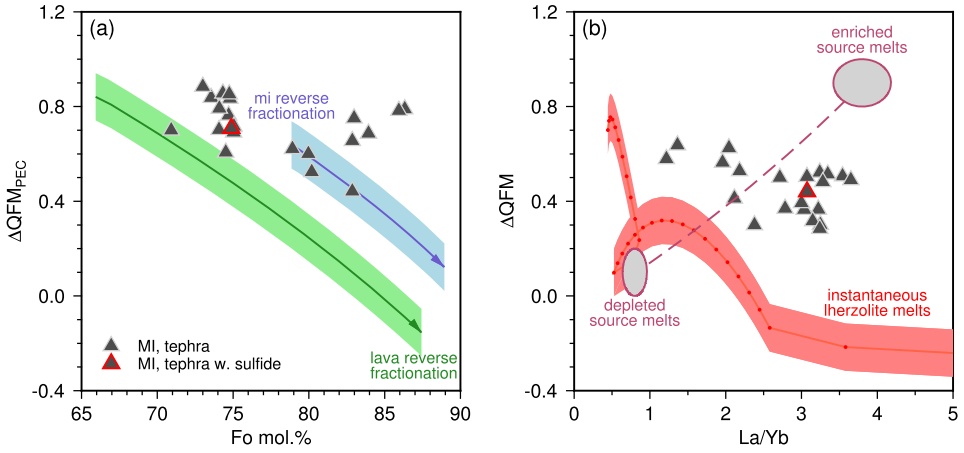

Fig. 10. (a) Comparison of Laki tephra-hosted melt inclusion fO_2 (corrected for post-entrapment crystallisation) with the expected variation in fO_2 during fractional crystallisation. We used Petrolog3 (Danyushevsky and Plechov, 2011) to model fractional crystallisation starting from the major element composition of a Laki lava glass (shown in green) and a tephra-hosted inclusion (shown in blue). Pressure was set to 2 kbar and we used the mineral-melt models of Langmuir et al. (1992). Partition coefficients were $D_{olv}^{Fe_2O_3} = 0$, $D_{plg}^{Fe_2O_3} = 0$ and $D_{cpx}^{Fe_2O_3} = 0.453$ (Mallmann and O'Neill, 2009). Aside from crystal fractionation, the system was unbuffered and closed to oxygen exchange. (b) Comparison of fO_2 and trace element variability in Laki tephra-hosted inclusions, both corrected to 10 wt.% MgO, with that expected from mixing of enriched and depleted primary melts of the Icelandic mantle source. Endmember enriched and depleted melt La/Yb is from Shorttle et al. (2014) and fO_2 from Shorttle et al. (2015); values are provided in Table A.2. In red we show calculated instantaneous fractional melt compositions from lherzolitic mantle (Workman and Hart, 2005) at a mantle potential temperature of 1390 °C; points indicate pressure intervals of 0.05 GPa during decompression melting. Calculations were performed using the pMELTS model (Ghiorso et al., 2002) implemented through alphaMELTS (Smith and Asimow, 2005; Thompson et al., 2007). (For interpretation of the colours in this figure, the reader is referred to the web version of this article.)

A suite of 65 olivine-hosted melt inclusions and 9 matrix glasses from the AD 1783 Laki eruption, Iceland, exhibit changes in oxidation state that represent the progressive reduction of the pre-eruptive magma in response to sulfur degassing. Melt inclusions from rapidly quenched tephra samples have higher $Fe^{3+}/\Sigma Fe$ by up to 0.08 and higher ΔQFM by up to 1.3 $\log(fO_2)$ units than melt inclusions from lava selvages. The tephra-hosted inclusions have an average $Fe^{3+}/\Sigma Fe$ of 0.206, and represent the redox conditions of the pre-eruptive Laki magma. In contrast, the lava-hosted inclusions have experienced diffusive modification of both fO_2 and H_2O during lava transport. The modifications of fO_2 and H_2O occur at somewhat different rates, but in both cases complete re-equilibration between the inclusions and their external environment occurs within hours to days.

Redox changes in the Laki magma are controlled by the outgassing of sulfur, which both reduces the carrier lava and decreases the sulfur content at sulfide saturation. Diffusive reduction of fO_2 drives sulfide saturation in the lava-hosted melt inclusions, and the formation of immiscible sulfide globules reduces the residual S content and S/Sm ratio in the silicate glass. In contrast, tephra-hosted inclusions are quenched sufficiently quickly to preserve the S contents and S/Sm ratios of the melt at the point of inclusion entrapment.

The rapid modification of $Fe^{3+}/\Sigma Fe$ and fO_2 that occurs as melt inclusions approach equilibrium with their external environment means that any redox heterogeneity present at the time of melt inclusion trapping was overprinted during the concurrent mixing and crystallisation of the diverse primary melts that fed the Laki magmatic system. However, olivine-hosted melt inclusions are reliable archives of pre-eruptive magmatic redox conditions at the final pressure and temperature of magma equilibration and storage, provided that the inclusions are rapidly quenched upon eruption. Applying a fractionation correction to 10 wt.% MgO, the Laki primary melt is deduced to have $Fe^{3+}/\Sigma Fe$ of 0.18 ± 0.02. This ferric iron content is much higher than the $Fe^{3+}/\Sigma Fe$ of 0.10, and ΔQFM-1, that has often been assumed for Icelandic basalts, and indicates that Icelandic melts are more oxidised than mid-ocean ridge basalt ($Fe^{3+}/\Sigma Fe = 0.10$–0.16 (Cottrell and Kelley, 2011)). This difference between Iceland and mid-ocean ridge basalts is consistent with transport of oxidised material into the mantle, which is then sampled in certain ocean islands with strong signatures of recycled material.

Acknowledgements

We thank Diamond Light Source for access to beamline I18 under proposals SP9456 and SP12130, and especially beamline scientist Konstantin Ignatyev for his assistance during the analytical work. We thank the Smithsonian Institution National Museum of Natural History for the loan of NMNH 117393. MEH acknowledges support from a Junior Research Fellowship at Murray Edwards College, Cambridge. OS is supported by a Title A Fellowship from Trinity College, Cambridge. JM was supported by NERC grant NE/J021539/1. We thank Marc Hirschmann and an anonymous reviewer for their constructive comments, and Tamsin Mather for editorial handling.

Appendix A. Additional tables and figures

Table A.1
Step sizes and dwell times used for XANES Fe K-edge analyses.

Energy range (eV)	Step size (eV)	Dwell time (s)
7000.0–7100.0	10.0	1
7101.0–7104.0	1.0	2
7104.1–7110.0	0.1	5
7110.1–7118.0	0.1	10
7118.1–7119.4	0.1	5
7119.5–7127.0	0.5	2
7128.0–7144.0	1.0	2
7148.0–7410.0	4.0	2
7410.0–7500.0	10.0	1

Table A.2
Compositions of enriched and depleted source melts used in Fig. 10.

Source melt	La/Yb	Nb/Zr	$Fe_2O_{3(Fo90)}$ wt.%	ΔQFM
Enriched	3.812	0.155	1.8–2.0	0.9
Depleted	0.821	0.034	1.5	0.1

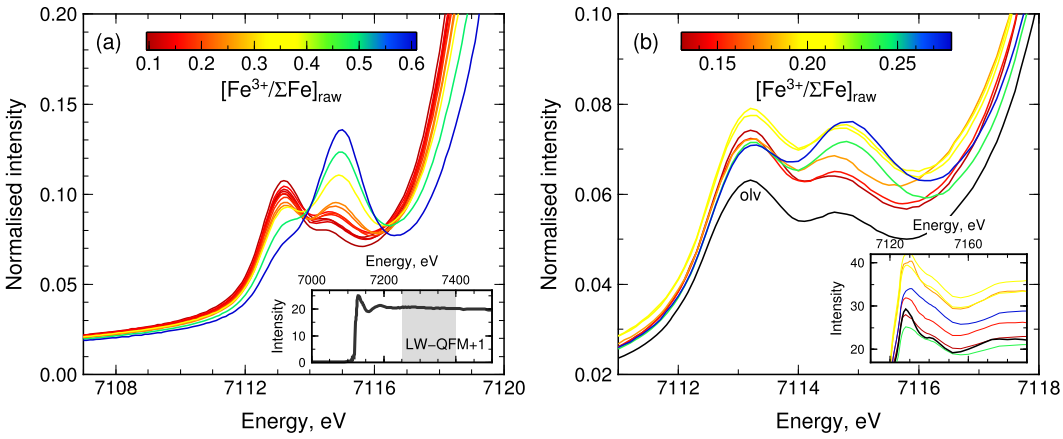

Fig. A.1. (a) Edge step-normalised intensity vs. energy for standards from the NMNH 117393 reference block (Cottrell et al., 2009), showing the spectra over the energy range of the pre-edge region used in fitting both standards and samples. Spectra for the standards are coloured by their reference $Fe^{3+}/\Sigma Fe$ values as determined by Mössbauer spectroscopy. Inset: Raw, un-normalised spectrum of one standard glass over the full energy range analysed, with the energy range used for normalisation shaded in grey. (b) Edge step-normalised intensity vs. energy for representative Laki melt inclusions, coloured by their measured $Fe^{3+}/\Sigma Fe$ values as calibrated using the NMNH standards. The black line labelled 'olv' is a melt inclusion analysis contaminated by the host olivine. Inset: Raw, un-normalised spectra for the same Laki melt inclusions, showing the post-edge shoulder. Note the structure at ~7140 eV in the olivine-contaminated spectrum. (For interpretation of the colours in this figure, the reader is referred to the web version of this article.)

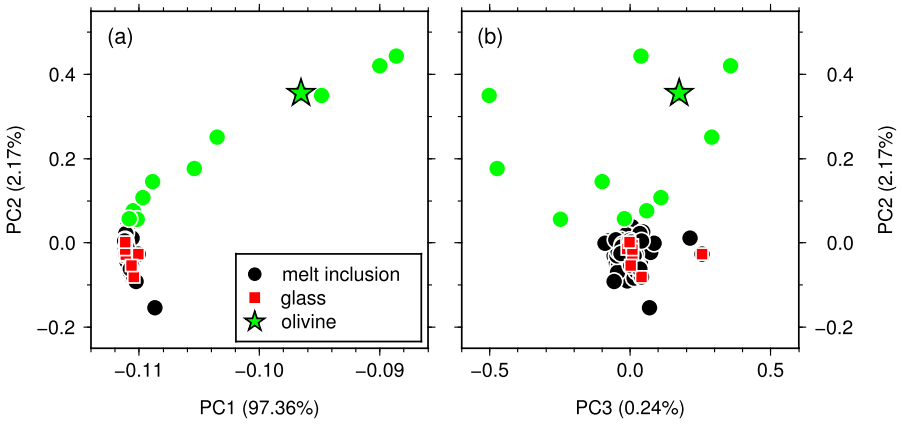

Fig. A.2. Principal component (PC) analysis of normalised XANES spectra over the energy interval 7127–7300 eV. Melt inclusion and glass analyses are shown by circles and squares respectively. The green star is an olivine analysis. The first principal component describes 97% of the variability in this energy range. A high PC2 score is indicative of olivine contamination. Melt inclusion analyses from further consideration on the basis of olivine contamination are plotted in green. (For interpretation of the colours in this figure, the reader is referred to the web version of this article.)

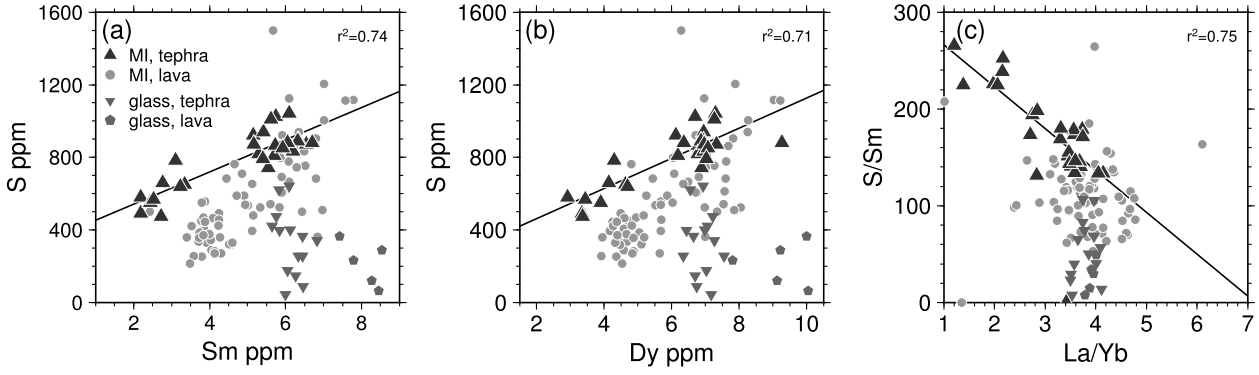

Fig. A.3. Sulfur and trace element variability in Laki melt inclusions. Correlations and correlation coefficients are shown for tephra-hosted melt inclusions.

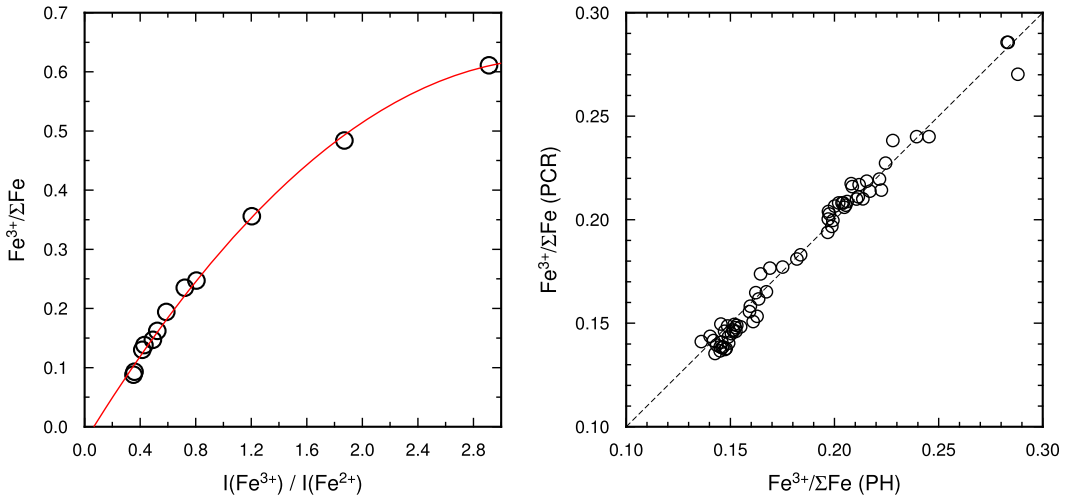

Fig. B.1. (a) Calibration curve for the NMNH standards based on the peak height ratio, $I(Fe^{3+})/I(Fe^{2+})$. (b) Comparison of the principal component regression (PCR) calibration with the peak height ratio (PH) calibration. A near 1:1 correlation is observed for $Fe^{3+}/\Sigma Fe$ determined on the Laki melt inclusions and glasses using the two methods.

Appendix B. Comparison of XANES calibration methods

We compared our PCR calibration with alternative calibration methods that use the centroid energy, peak area ratio or peak height ratio as a proxy for $Fe^{3+}/\Sigma Fe$ (Berry et al., 2003; Cottrell et al., 2009; Zhang et al., 2016; Fiege et al., 2017). We extracted the relevant pre-edge spectral features by simultaneously fitting a baseline consisting of a linear function and a damped harmonic oscillator function, and two Gaussian functions to describe pre-edge peaks. Reference glass spectra were then used to establish calibration curves based on centroid energy, peak area ratio and peak height ratio, and hence determine $Fe^{3+}/\Sigma Fe$ in the unknown samples. Using returned $Fe^{3+}/\Sigma Fe$ in the unknowns to compare the calibration methods, we find near-perfect linear correlations between the PCR method and the three calibrations based on peak fitting procedures (Fig. B.1). The choice of calibration method therefore has a negligible effect on our results, particularly given that the variability in our dataset is much larger than any systematic differences between the calibration procedures.

Appendix C. Mössbauer calibration of XANES standards

The PCR calibration used in this study is based on the $Fe^{3+}/\Sigma Fe$ values for the National Museum of Natural History's basaltic glass standards reported by Cottrell et al. (2009), who measured $Fe^{3+}/\Sigma Fe$ in these glasses by room temperature Mössbauer spectroscopy. There has been recent debate over the potential influence of recoilless fraction on the area ratios of the absorption doublets associated with Fe^{2+} and Fe^{3+} in room temperature (RT) Mössbauer spectra of silicate glasses. New cryogenic (10 K) Mössbauer spectra of the NMNH glasses suggest that recoilless fraction effects can be accounted for by applying a correction factor C of 1.1 (Hirschmann et al., 2015), where:

$$[Fe^{3+}/\Sigma Fe]_{corrected} = [Fe^{3+}/\Sigma Fe]_{RT}/\{[Fe^{3+}/\Sigma Fe]_{RT} + C(1 - [Fe^{3+}/\Sigma Fe]_{RT})\} \quad (7)$$

Cottrell and Kelley (2011) used the room temperature calibration of the NMNH standards to show that the global average $Fe^{3+}/\Sigma Fe$ of MORB glasses is 0.16 ± 0.01, but if the correction factor above is applied to XANES data then the median $Fe^{3+}/\Sigma Fe$ in MORB is ~0.15 (Hirschmann et al., 2015). In light of this, Helz et al. (2017) elected to correct measured $Fe^{3+}/\Sigma Fe$ values by −0.01 (absolute) relative to the Cottrell et al. (2009) calibration. We have chosen not to apply this correction factor, in order to better compare our results with previous XANES measurements reported according to the original Cottrell et al. (2009) calibration. We emphasise that our main focus is on relative differences in $Fe^{3+}/\Sigma Fe$ between samples, which are unambiguously resolved by the precision of the XANES measurements and are independent of systematic shifts caused by the accuracy of the calibration method.

Appendix D. Supplementary material

Supplementary material related to this article can be found online at http://dx.doi.org/10.1016/j.epsl.2017.09.029.

References

Allègre, C.J., Turcotte, D.L., 1986. Implications of a two-component marble-cake mantle. Nature 323, 123–127.
Berry, A.J., Danyushevsky, L.V., O'Neill, H.S.C., Newville, M., Sutton, S.R., 2008. Oxidation state of iron in komatiitic melt inclusions indicates hot Archaean mantle. Nature 455, 960–963.
Berry, A.J., O'Neill, H.S.C., Jayasuriya, K.D., Campbell, S.J., Foran, G.J., 2003. XANES calibrations for the oxidation state of iron in a silicate glass. Am. Mineral. 88, 967–977.
Botcharnikov, R.E., Koepke, J., Holtz, F., McCammon, C., Wilke, M., 2005. The effect of water activity on the oxidation and structural state of Fe in a ferro-basaltic melt. Geochim. Cosmochim. Acta 69, 5071–5085.
Brounce, M., Feineman, M., LaFemina, P., Gurenko, A., 2012. Insights into crustal assimilation by Icelandic basalts from boron isotopes in melt inclusions from the 1783–1784 Lakagígar eruption. Geochim. Cosmochim. Acta 94, 164–180.
Brounce, M.N., Kelley, K.A., Cottrell, E., 2014. Variations in $Fe^{3+}/\Sigma Fe$ of Mariana arc basalts and mantle wedge fO_2. J. Petrol. 55, 2513–2536.
Bucholz, C.E., Gaetani, G.A., Behn, M.D., Shimizu, N., 2013. Post-entrapment modification of volatiles and oxygen fugacity in olivine-hosted melt inclusions. Earth Planet. Sci. Lett. 374, 145–155.
Burgisser, A., Scaillet, B., 2007. Redox evolution of a degassing magma rising to the surface. Nature 445, 194–197.
Chen, Y., Provost, A., Schiano, P., Cluzel, N., 2011. The rate of water loss from olivine-hosted melt inclusions. Contrib. Mineral. Petrol. 162, 625–636.
Cherniak, D.J., 2010. REE diffusion in olivine. Am. Mineral. 95, 362–368.
Cottrell, E., Kelley, K.A., 2011. The oxidation state of Fe in MORB glasses and the oxygen fugacity of the upper mantle. Earth Planet. Sci. Lett. 305, 270–282.
Cottrell, E., Kelley, K.A., Lanzirotti, A., Fischer, R.A., 2009. High-precision determination of iron oxidation state in silicate glasses using XANES. Chem. Geol. 268, 167–179.
Czamanske, G.K., Moore, J.G., 1977. Composition and phase chemistry of sulfide globules in basalt from the Mid-Atlantic Ridge rift valley near 37°N lat. Geol. Soc. Am. Bull. 88, 587–599.
Danyushevsky, L.V., Plechov, P., 2011. Petrolog3: integrated software for modeling crystallization processes. Geochem. Geophys. Geosyst. 12, 1–32. http://dx.doi.org/10.1029/2011GC003516.
Demouchy, S., Mackwell, S., 2006. Mechanisms of hydrogen incorporation and diffusion in iron-bearing olivine. Phys. Chem. Miner. 33, 347–355.

Dohmen, R., Chakraborty, S., 2007. Fe-Mg diffusion in olivine II: point defect chemistry, change of diffusion mechanisms and a model for calculation of diffusion coefficients in natural olivine. Phys. Chem. Miner. 34, 409–430.
Dungan, M.A., Rhodes, J.M., 1978. Residual glasses and melt inclusions in basalts from DSDP Legs 45 and 46: evidence for magma mixing. Contrib. Mineral. Petrol. 67, 417–431.
Fiege, A., Ruprecht, P., Simon, A.C., Bell, A.S., Göttlicher, J., Newville, M., Lanzirotti, T., Moore, G., 2017. Calibration of Fe XANES for high-precision determination of Fe oxidation state in glasses: comparison of new and existing results obtained at different synchrotron radiation sources. Am. Mineral. 102, 369–380.
Fortin, M.-A., Riddle, J., Desjardins-Langlais, Y., Baker, D.R., 2015. The effect of water on the sulfur concentration at sulfide saturation (SCSS) in natural melts. Geochim. Cosmochim. Acta 160, 100–116.
Frost, B.R., 1991. Introduction to oxygen fugacity and its petrologic importance. Rev. Mineral. Geochem. 25, 1–9.
Gaetani, G.A., 2016. The behavior of $Fe^{3+}/\Sigma Fe$ during partial melting of spinel lherzolite. Geochim. Cosmochim. Acta 185, 64–77.
Gaetani, G.A., O'Leary, J.A., Shimizu, N., Bucholz, C.E., Newville, M., 2012. Rapid reequilibration of H_2O and oxygen fugacity in olivine-hosted melt inclusions. Geology 40, 915–918.
Gaetani, G.A., Watson, E.B., 2002. Modeling the major-element evolution of olivine-hosted melt inclusions. Chem. Geol. 183, 25–41.
Gaillard, F., Scaillet, B., Arndt, N.T., 2011. Atmospheric oxygenation caused by a change in volcanic degassing pressure. Nature 478, 229–232.
Gaillard, F., Schmidt, B., Mackwell, S., McCammon, C., 2003. Rate of hydrogen–iron redox exchange in silicate melts and glasses. Geochim. Cosmochim. Acta 67, 2427–2441.
Ghiorso, M.S., Hirschmann, M.M., Reiners, P.W., Kress, V.C., 2002. The pMELTS: a revision of MELTS for improved calculation of phase relations and major element partitioning related to partial melting of the mantle to 3 GPa. Geochem. Geophys. Geosyst. 3, 1–35.
Guilbaud, M.-N., Blake, S., Thordarson, T., Self, S., 2007. Role of syn-eruptive cooling and degassing on textures of lavas from the AD 1783–1784 Laki eruption, south Iceland. J. Petrol. 48, 1265–1294.
Hartley, M.E., Maclennan, J., Edmonds, M., Thordarson, T., 2014. Reconstructing the deep CO_2 degassing behaviour of large basaltic fissure eruptions. Earth Planet. Sci. Lett. 393, 120–131.
Hartley, M.E., Morgan, D.J., Maclennan, J., Edmonds, M., Thordarson, T., 2016. Tracking timescales of short-term precursors to large basaltic fissure eruptions through Fe–Mg diffusion in olivine. Earth Planet. Sci. Lett. 439, 58–70.
Hartley, M.E., Neave, D.A., Maclennan, J., Edmonds, M., Thordarson, T., 2015. Diffusive over-hydration of olivine-hosted melt inclusions. Earth Planet. Sci. Lett. 425, 168–178.
Hartley, M.E., Thordarson, T., 2013. The 1874–76 volcano-tectonic episode at Askja, North Iceland: lateral flow revisited. Geochem. Geophys. Geosyst. 14, 2286–2309. http://dx.doi.org/10.1002/ggge.20151.
Helz, R.T., Cottrell, E., Brounce, M.N., Kelley, K.A., 2017. Olivine-melt relationships and syneruptive redox variations in the 1959 eruption of Kīlauea Volcano as revealed by XANES. J. Volcanol. Geotherm. Res. 333–334, 1–14.
Hirschmann, M.M., Zhang, H., Cottrell, E., 2015. Revised Mossbauer calibration for Fe^{3+}/Fe^{T} of XANES basalt standards: implications for MORB. AGU Fall Meeting Abstracts. V31D–3049.
Iacono-Marziano, G., Morizet, Y., Le Trong, E., Gaillard, F., 2012. New experimental data and semi-empirical parameterization of H_2O–CO_2 solubility in mafic melts. Geochim. Cosmochim. Acta 97, 1–23.
Jugo, P.J., 2009. Sulfur content at sulfide saturation in oxidized magmas. Geology 37, 415–418.
Jugo, P.J., Wilke, M., Botcharnikov, R.E., 2010. Sulfur K-edge XANES analysis of natural and synthetic basaltic glasses: implications for S speciation and S content as function of oxygen fugacity. Geochim. Cosmochim. Acta 74, 5926–5938.
Kent, A.J.R., 2008. Melt inclusions in basaltic and related volcanic rocks. Rev. Mineral. Geochem. 69, 273–331.
Kilinc, A., Carmichael, I.S.E., Rivers, M.L., Sack, R.O., 1983. The ferric–ferrous ratio of natural silicate liquids equilibrated in air. Contrib. Mineral. Petrol. 83, 136–140.
Kohlstedt, D.L., Mackwell, S.J., 1998. Diffusion of hydrogen and intrinsic point defects in olivine. Z. Phys. Chem. 207, 147–162.
Kress, V.C., Carmichael, I.S.E., 1991. The compressibility of silicate liquids containing Fe_2O_3 and the effect of composition, temperature, oxygen fugacity and pressure on their redox states. Contrib. Mineral. Petrol. 108, 82–92.
Langmuir, C.H., Klein, E.M., Plank, T., 1992. Petrological constraints on melt formation and migration beneath mid-ocean ridges. In: Phipps Morgan, J., Blackman, D., Sinton, J.L. (Eds.), Geophysical Monograph, vol. 71. American Geophysical Union, pp. 183–280.
Liu, Y., Samaha, N.-T., Baker, D.R., 2007. Sulfur concentration at sulfide saturation (SCSS) in magmatic silicate melts. Geochim. Cosmochim. Acta 71, 1783–1799.
Lowenstern, J.B., 1995. Applications of silicate-melt inclusions to the study of magmatic volatiles. In: Thompson, J.F.H. (Ed.), Magmas, Fluids and Ore Deposits. In: Mineralogical Association of Canada Short Course, vol. 23, pp. 71–99.
Maclennan, J., 2008a. Concurrent mixing and cooling of melts under Iceland. J. Petrol. 49, 1931–1953.
Maclennan, J., 2008b. Lead isotope variability in olivine-hosted melt inclusions from Iceland. Geochim. Cosmochim. Acta 72, 4159–4176.
Maclennan, J., McKenzie, D., Grönvold, K., Shimizu, N., Eiler, J.M., Kitchen, N., 2003. Melt mixing and crystallization under Theistareykir, northeast Iceland. Geochem. Geophys. Geosyst. 4, 8624. http://dx.doi.org/10.1029/2003GC000558.
Mallmann, G., O'Neill, H.S.C., 2009. The crystal/melt partitioning of V during mantle melting as a function of oxygen fugacity compared with some other elements (Al, P, Ca, Sc, Ti, Cr, Fe, Ga, Y, Zr and Nb). J. Petrol. 50, 1765–1794.
Matjuschkin, V., Blundy, J.D., Brooker, R.A., 2016. The effect of pressure on sulphur speciation in mid-to deep-crustal arc magmas and implications for the formation of porphyry copper deposits. Contrib. Mineral. Petrol. 171, 1–25.
Mavrogenes, J.A., O'Neill, H.S.C., 1999. The relative effects of pressure, temperature and oxygen fugacity on the solubility of sulfide in mafic magmas. Geochim. Cosmochim. Acta 63, 1173–1180.
Métrich, N., Sigurdsson, H., Meyer, P.S., Devine, J.D., 1991. The 1783 Lakagigar eruption in Iceland – geochemistry, CO_2 and sulfur degassing. Contrib. Mineral. Petrol. 107, 435–447.
Métrich, N., Wallace, P.J., 2008. Volatile abundances in basaltic magmas and their degassing paths tracked by melt inclusions. Rev. Mineral. Geochem. 69, 363–402.
Moussallam, Y., Edmonds, M., Scaillet, B., Peters, N., Gennaro, E., Sides, I., Oppenheimer, C., 2016. The impact of degassing on the oxidation state of basaltic magmas: a case study of Kīlauea volcano. Earth Planet. Sci. Lett. 450, 317–325.
Moussallam, Y., Oppenheimer, C., Scaillet, B., Gaillard, F., Kyle, P., Peters, N., Hartley, M., Berlo, K., Donovan, A., 2014. Tracking the changing oxidation state of Erebus magmas, from mantle to surface, driven by magma ascent and degassing. Earth Planet. Sci. Lett. 393, 200–209.
Mungall, J.E., Su, S., 2005. Interfacial tension between magmatic sulfide and silicate liquids: constraints on kinetics of sulfide liquation and sulfide migration through silicate rocks. Earth Planet. Sci. Lett. 234, 135–149.
Nakamura, A., Schmalzried, H., 1983. On the nonstoichiometry and point defects of olivine. Phys. Chem. Miner. 10, 27–37.
Neave, D.A., Hartley, M.E., Maclennan, J., Edmonds, M., Thordarson, T., 2017. Volatile and light lithophile elements in high-anorthite plagioclase-hosted melt inclusions from Iceland. Geochim. Cosmochim. Acta 205, 100–118.
Neave, D.A., Maclennan, J., Edmonds, M., Thordarson, T., 2014. Melt mixing causes negative correlation of trace element enrichment and CO_2 content prior to an Icelandic eruption. Earth Planet. Sci. Lett. 400, 272–283.
Neave, D.A., Passmore, E., Maclennan, J., Fitton, G., Thordarson, T., 2013. Crystal-melt relationships and the record of deep mixing and crystallization in the AD 1783 Laki eruption, Iceland. J. Petrol. 54, 1661–1690.
Newman, S., Lowenstern, J.B., 2002. VolatileCalc: a silicate melt-H_2O–CO_2 solution model written in Visual Basic for excel. Comput. Geosci. 28, 597–604.
Nichols, A.R.L., Carroll, M.R., Hóskuldsson, A., 2002. Is the Iceland hot spot also wet? Evidence from the water contents of undegassed submarine and subglacial pillow basalts. Earth Planet. Sci. Lett. 202, 77–87.
O'Neill, H.S.C., Jenner, F.E., 2012. The global pattern of trace-element distributions in ocean floor basalts. Nature 491, 698–704.
O'Neill, H.S.C., Mavrogenes, J.A., 2002. The sulfide capacity and the sulfur content at sulfide saturation of silicate melts at 1400 °C and 1 bar. J. Petrol. 43, 1049–1087.
Óskarsson, N., Helgason, O., Steinthórsson, S., 1994. Oxidation-state of iron in mantle-derived magmas of the Icelandic rift-zone. Hyperfine Interact. 91, 733–737.
Passmore, E., Maclennan, J., Fitton, G., Thordarson, T., 2012. Mush disaggregation in basaltic magma chambers: evidence from the AD 1783 Laki eruption. J. Petrol. 53, 2593–2623.
Portnyagin, M., Almeev, R., Matveev, S., Holtz, F., 2008. Experimental evidence for rapid water exchange between melt inclusions in olivine and host magma. Earth Planet. Sci. Lett. 272, 541–552.
Qin, Z., Lu, F., Anderson, A.T., 1992. Diffusive reequilibration of melt and fluid inclusions. Am. Mineral. 77, 565–576.
Saal, A.E., Hauri, E.H., Langmuir, C.H., Perfit, M.R., 2002. Vapour undersaturation in primitive mid-ocean-ridge basalt and the volatile content of Earth's upper mantle. Nature 419, 451–455.
Shorttle, O., Maclennan, J., 2011. Compositional trends of Icelandic basalts: implications for short-length scale lithological heterogeneity in mantle plumes. Geochem. Geophys. Geosyst. 12, Q11008. http://dx.doi.org/10.1029/2011GC003748.
Shorttle, O., Maclennan, J., Lambart, S., 2014. Quantifying lithological variability in the mantle. Earth Planet. Sci. Lett. 395, 24–40.
Shorttle, O., Moussallam, Y., Hartley, M.E., Maclennan, J., Edmonds, M., Murton, B.J., 2015. Fe-XANES analyses of Reykjanes Ridge basalts: implications for oceanic crust's role in the solid Earth oxygen cycle. Earth Planet. Sci. Lett. 427, 272–285.
Shorttle, O., Rudge, J.F., Maclennan, J., Rubin, K.H., 2016. A statistical description of concurrent mixing and crystallization during MORB differentiation: implications for trace element enrichment. J. Petrol. 1, 33.
Slater, L., McKenzie, D., Grönvold, K., Shimizu, N., 2001. Melt generation and movement beneath Theistareykir, NE Iceland. J. Petrol. 42, 321–354.
Smith, P.M., Asimow, P.D., 2005. Adiabat_1ph: a new public front-end to the MELTS, pMELTS, and pHMELTS models. Geochem. Geophys. Geosyst. 6.

Sobolev, A.V., 1996. Melt inclusions in minerals as a source of principle petrological information. Petrology 4, 209–220.
Sobolev, A.V., Shimizui, N., 1993. The Mid-Atlantic Ridge. Nature 363, 13.
Thompson, R.N., Riches, A.J.V., Antoshechkina, P.M., Pearson, D.G., Nowell, G.M., Ottley, C.J., Dickin, A.P., Hards, V.L., Nguno, A.-K., Niku-Paavola, V., 2007. Origin of CFB magmatism: multi-tiered intracrustal picrite-rhyolite magmatic plumbing at Spitzkoppe, western Namibia, during early Cretaceous Etendeka magmatism. J. Petrol. 48, 1119–1154.
Thordarson, T., Self, S., 1993. The Laki (Skaftár Fires) and Grímsvötn eruptions in 1783–1785. Bull. Volcanol. 55, 233–263.
Thordarson, T., Self, S., Óskarsson, N., Hulsebosch, T., 1996. Sulfur, chlorine, and fluorine degassing and atmospheric loading by the 1783–1784 AD Laki (Skaftár fires) eruption in Iceland. Bull. Volcanol. 58, 205–225.
Wanamaker, B.J., 1994. Point defect diffusivites in San Carlos olivine derived from reequilibration of electrical conductivity following changes in oxygen fugacity. Geophys. Res. Lett. 21, 21–24.
Wilke, M., Klimm, K., Kohn, S.C., 2011. Spectroscopic studies on sulfur speciation in synthetic and natural glasses. Rev. Mineral. Geochem. 73, 41–78.
Winpenny, B., Maclennan, J., 2011. A partial record of mixing of mantle melts preserved in Icelandic phenocrysts. J. Petrol. 52, 1791–1812.
Workman, R.K., Hart, S.R., 2005. Major and trace element composition of the depleted MORB mantle (DMM). Earth Planet. Sci. Lett. 231, 53–72.
Zhang, H.L., Hirschmann, M.M., Cottrell, E., Newville, M., Lanzirotti, A., 2016. Structural environment of iron and accurate determination of $Fe^{3+}/\Sigma Fe$ ratios in andesitic glasses by XANES and Mössbauer spectroscopy. Chem. Geol. 428, 48–58.